Towards an Improved Electrocatalytic Material for Detection of Polyphenols Based on Transition Metal Phosphides Anchored on Reduced Graphene Oxide

Isilda Amorim[1,2], Zhipeng Yu[2], Fátima Bento[1,z] and Lifeng Liu[2,z]

[1]Centre of Chemistry, University of Minho, Gualtar Campus, Braga, 4710-057, Portugal;
[2]Clean Energy Cluster, International Iberian Nanotechnology Laboratory (INL), Avenida Mestre Jose Veiga, 4715-330 Braga, Portugal
[z]E-mail Address: lifeng.liu@inl.int; fbento@quimica.uminho.pt

Abstract

The design of advanced materials with catalytic activity for detection of a target molecule is key to construct a sensitive electrochemical sensor. Transition metal phosphides (TMPs) have recently attracted substantial interest and are widely investigated as electrode material in the field of energy conversion/storage. TMPs have also been exploited for electrochemical sensing showing promising results for molecular detection. In this work, we report the preparation of a composite consisting of bimetallic cobalt−nickel phosphide (CoNiP) nanoparticles supported on reduced graphene oxide (rGO) and study the impact of phosphorization and presence of rGO on the electrochemical response using hydroquinone (HQ) as a model phenolic compound. The results show that the catalytic performance of CoNiP@rGO is a consequence of the synergetic interaction between different atoms of CoNiP and rGO, where P increases the proton concentration at the electrode interface favoring a catalytic mechanism where metal centers are oxidized. In the presence of rGO this effect is suppressed due to the formation of high valence states of CoNiP. The remarkable electrocatalytic performance may originate from the modulation of the electronic structure together with the large electroactive surface area and low electron-transfer resistance, enabling CoNiP@rGO to be a promising candidate for electrochemical sensor construction.

Introduction

The development of electrocatalytic materials for electrode design is of critical importance in the construction of advanced electrochemical sensors for target molecule detection. From an electrode materials standpoint, several transition metal (TM) based electrocatalysts such as oxides and hydroxides have been reported as efficient materials for the detection of target analytes. For instance, CuO nanoparticles[1] and graphite decorated with PdO@C[2] have been studied for detection of pesticides and phenolic compounds. However, oxide and hydroxide materials usually suffer from poor electrical conductivity. Therefore, a variety of transition metal based electrocatalysts such as sulfides, selenides and phosphides, including $CoFeSe_2$[3], MoCuSe[4], CuS[5], have been explored for molecular sensing of caffeic acid, bisphenol A and H_2O_2, respectively, because TM chalcogenides and phosphides are metalloid and show substantially higher electrical conductivity than TM oxides and hydroxides. Among these emerging catalysts, transition metal phosphides (TMPs) have recently attracted considerable attention, representing an important class of compounds with inherent advantages. Due to their metalloid characteristics, good structural stability as well as natural abundance and low-cost[6] they have been extensively studied for applications in electrochemical energy storage and conversion, *e.g.* water splitting[7-9] and supercapacitors[10-12].

Additionally, anchoring TM-based catalysts on carbonaceous nanomaterials has been reported to be an effective strategy to improve the stability and to avoid the dissolution or agglomeration of electrode materials[13-15]. Up to now, various carbon materials have been widely exploited as promising supportive and/or active materials, such as carbon nanotube (CNT), carbon nanofiber (CNF), graphene, carbon nanosphere and activated carbon[16-18]. In particular, graphene emerged as a star material in the field of materials science due to its outstanding properties including high chemical stability, large specific surface area and superior electrical and thermal conductivity[19, 20]. The reduction of graphene oxide (GO), an oxidized form of graphene which contains hydrophilic functional groups, is an efficient way to produce graphene powders on a large scale. The removal of oxygen functional groups of GO to produce the so-called reduced graphene oxide (rGO) can be carried out using different approaches, for example by chemical, photo-mediated, thermal and electrochemical reduction[21]. Taking advantage of the graphene's properties, the electrochemical performance

of TMP-based electrode materials is expected to be improved by supporting TMP on rGO, due to the strong metal-support interactions that may cause electron transfer at the metal/graphene interface[22], improving the electrical conductivity and regulating the electronic state of TMP nanoparticles.

Recent research also indicates that TMPs can be used as efficient electrode materials for molecular detection. For example, TMPs such as CoP/GCE[23], Ni_2P/CC[24], Cu_3P/CF[25] and NiCoP/GCE[26], showed remarkable performance towards glucose oxidation under alkaline conditions with high sensitivities (0.12 − 11.4 A M^{-1} cm^{-2}), holding promise for use in non-enzymatic sensors. The TMPs' effectiveness was also demonstrated for electrochemical enzymeless detection of H_2O_2[27-30] with very low detection limits (2 nM − 0.65 μM) under physiological conditions. Moreover, molecules such as dopamine[31] and chloramphenicol[32], among others[33, 34], could also be sensitively detected using this class of catalysts. To the best of our knowledge, only a few works reports the use of monometallic TMPs as electrode material for the detection of phenolic substances[34-37], despite the importance of this class of substances as environmental contaminants. Phenolic compounds are among the chemicals of major concern as they tend to persist in the environment over a long period of time, accumulate and exert toxic effects on humans and animals[38, 39]. Due to their toxicity, many phenolic compounds have been designated as priority pollutants by the US Environmental Protection Agency (US EPA) and European Commission (EC)[40]. For efficient control of water quality, particularly in developing countries, the design of advanced materials that have good catalytic activity for phenolic compounds and are simultaneously accessible is relevant[41]. The mass production of affordable sensors for water quality monitoring is required for both environmental protection and public health. TMPs are good candidates for electrode material due to its good electrochemical properties and low-cost.

While various mono-metallic TMPs have been investigated for electrochemical sensors, recent studies have demonstrated that doping mono-metallic TMPs with a secondary transition metal can markedly improve the electrochemical performance, due likely to the synergetic effect between different metal species, which possibly create lattice dislocation and defects, leading to an increase in active sites[42]. Given the outstanding performance of bimetallic

cobalt−nickel phosphide (CoNiP) as an active electrode material that has been proven for various applications both theoretically and experimentally[43, 44], in this work we report the synthesis of CoNiP nanoparticles supported on rGO (CoNiP@rGO). The electrochemical properties as electrode materials for a sensitive detection of phenolic compounds is demonstrated using the hydroquinone (HQ) as a probe molecule. The commercial glassy carbon modified with CoNiP@rGO showed the best electrochemical response with ten times higher current densities and lower peak-to-peak separation, among other catalysts tested, presenting a sensitivity of 35.7 A^{-1} M^{-1} cm^{-2}.

Experimental

Synthesis of cobalt−nickel precursor on rGO (CoNi@rGO). All chemicals used in this work were of analytical grade and were used as received. The material was synthesized by solution-based chemical reduction of corresponding metal cations in the presence of sodium borohydride ($NaBH_4$) in ethylene glycol (EG) solution [45]. In detail, 25 mL of GO solution (Sigma-Aldrich, 4 mg mL^{-1} in H_2O) was firstly mixed with 12.5 mL of EG and sonicated at 25 °C for 1 h. Subsequently, the EG solutions of $Co(NO_3)_2 \cdot 6H_2O$ (4.3 mL, 0.05 M) and $Ni(NO_3)_2 \cdot 6H_2O$ (4.3 mL, 0.05 M) were added, and the mixture was maintained under stirring for 3 h, at room temperature. Next, the solution temperature was increased to 60 °C and $NaBH_4$ solution (12.5 mL, 30 mg mL^{-1}) was slowly added under vigorous stirring. After reaction for 0.5 h, the mixture was cooled down to 25 °C, centrifuged, and rinsed several times with ultrapure water (18.2 MΩ cm). The as-obtained powders were dried in a vacuum oven at 80 °C. The unsupported cobalt−nickel precursor (CoNi) and pristine rGO used as controls were prepared according to the same procedure as described above using the corresponding precursor metal salts in the absence of GO and in the presence of GO but without the metal salts precursor, respectively.

Synthesis of CoNiP@rGO. The phosphorization was performed at 300 °C using NaH_2PO_2 as the source of phosphorus. Typically, 0.1 g of CoNi@rGO was loaded in a ceramic boat, with 0.5 g of NaH_2PO_2 placed 2 cm away from the CoNi@rGO at the upstream side. Subsequently, the boat was put into a tube furnace, wherein high-purity N_2 (99.999%) was purged at a flow

rate of 800 SCCM for 1 h to remove air. Afterwards, the furnace was ramped to 300 ^{o}C at a rate of 5 ^{o}C min^{-1}, held at this temperature for 2 h, and then cooled down naturally to room temperature. A constant N_2 flow was maintained in the whole process. The unsupported CoNiP was prepared according to the same procedure as described above, from unsupported CoNi precursor.

Materials characterization. Powder XRD examinations were conducted on a X'Pert PRO diffractometer (PANalytical) working at 45 kV and 40 mA with Cu Kα radiation (λ = 1.541874 Å) and a PIXcel detector. Data were collected with the Bragg-Brentano configuration in the 2θ range of 10 – 80^{o} at a scan speed of 0.01^{o} s^{-1}. X-ray photoelectron spectroscopy (XPS) characterization was performed on an ESCALAB 250 instrument with Al Kα X-rays (1489.6 eV). The morphology of all samples was examined by scanning electron microscopy (SEM, FEI Quanta 650). Transmission electron microscopy (TEM), high-resolution TEM (HRTEM), and scanning transmission electron microscopy (STEM) elemental mapping investigations were carried out on a probe-corrected transmission electron microscope operating at 200 kV (FEI Titan 80 – 200).

Electrode preparation and electrochemical measurements. The catalyst ink was prepared by ultrasonically dispersing 5 mg of catalysts into 1 mL of ultrapure water. To prepare an electrode, 5 μL of catalyst ink was loaded on a polished glassy carbon electrode (GCE) with an exposed geometric area of 0.07 cm^2, leading to a loading density of *ca.* 0.3 mg cm^{-2}. The electrode was then dried by exposing the surface of the modified electrode to an incandescent lamp. The electrochemical tests were carried out in a three-electrode configuration at room temperature using an Autolab PGSTAT 30 (Ecochemie) potentiostat controlled by the "General Purpose Electrochemical System" software, 4.9 version. The GCE loaded with the nanomaterials, a Pt wire and Ag/AgCl in saturated KCl solution were utilized as working, counter, and reference electrodes, respectively. 0.1 M of phosphate buffer solution (PBS) (pH = 7.0) was used as the supporting electrolyte. The electrochemical properties of the GCE loaded with various nanomaterials were characterized in 3.0 mM $K_3[Fe(CN)_6]$ solution containing 0.1 M KCl by recording the cyclic voltammetry (CV) curves from –0.1 to 0.5 V *vs*. Ag/AgCl at different scan rates (0.02 V s^{-1} to 0.4 V s^{-1}).

The electrochemical characterization towards hydroquinone (HQ) detection was performed by CV measurements conducted in 0.5 mM of HQ solution in 0.1 M PBS, at a scan rate (v) of 0.02 V s^{-1}. The electrochemical impedance spectroscopy (EIS) was measured in the same solution, where the frequency range was set from 10 mHz to 100 kHz with a signal amplitude of 10 mV using a Biologic VMP-3 potentiostat/galvanostat at room temperature. The differential pulse voltammetry (DPV) was performed from −0.2 to 0.3 V with a modulation amplitude of 25 mV and a step potential of 5 mV, with interval time of 0.5 s and modulation time of 0.05 s.

Results and Discussion

Characterization of the catalysts

The morphology and microstructure of CoNiP@rGO, prepared by chemical reduction of the corresponding transition metal cations and GO followed by a post-phosphorization treatment at 300 ºC, were firstly characterized by XRD and SEM. For comparison, other materials prepared as reference, including rGO, CoNi@rGO and CoNi, were also inspected.

Figs. 1a and **S1** show the XRD patterns of all materials prepared. The XRD patterns of CoNi@rGO and CoNi precursor are virtually featureless without any resolvable diffraction peaks owing likely to the small crystallite size while rGO show a wide diffraction peak at around 2θ = 18.7º, which can be attributed to (200) crystalline plane of carbon (ICDD No. 01-083-3673). After the phosphorization treatment, new diffraction peaks appear in both CoNiP and CoNiP@rGO that can be assigned to hexagonal CoNiP (ICDD No. 04-001-6153), confirming the formation of CoNiP solid solution. Some small impurities phases that appear in the XRD pattern of CoNiP@rGO (**Fig.1a**) can be attributed to $NaBH_4$ (ICDD 04-015-3244) and $NaBO_2.2H_2O$ (ICDD 00-006-0122) due to the use of $NaBH_4$ as reducing agent in the synthesis process. SEM images (**Fig. S2**) reveal smooth surfaces with wrinkles and folded regions for the as-received commercial GO (**Fig. S2a**), while reduced GO, *i.e.*, rGO, shows an aggregation degree higher than GO with crumpled features (**Fig. S2b**). After Co and Ni incorporation, the sheet-like structure and wrinkled pattern of rGO were retained (**Fig. S2c**), which could increase the contact area between the support and the nanoparticles. The CoNiP@rGO, formed through a controlled gas-solid phosphorization process, maintains the

sheet-like morphology with a very rough surface (**Fig. S2d**). On the other hand, the unsupported CoNi precursor and CoNiP, prepared in the absence of rGO support, presents a nanoparticle (NP) morphology with obvious agglomeration (**Fig. S2e-f**).

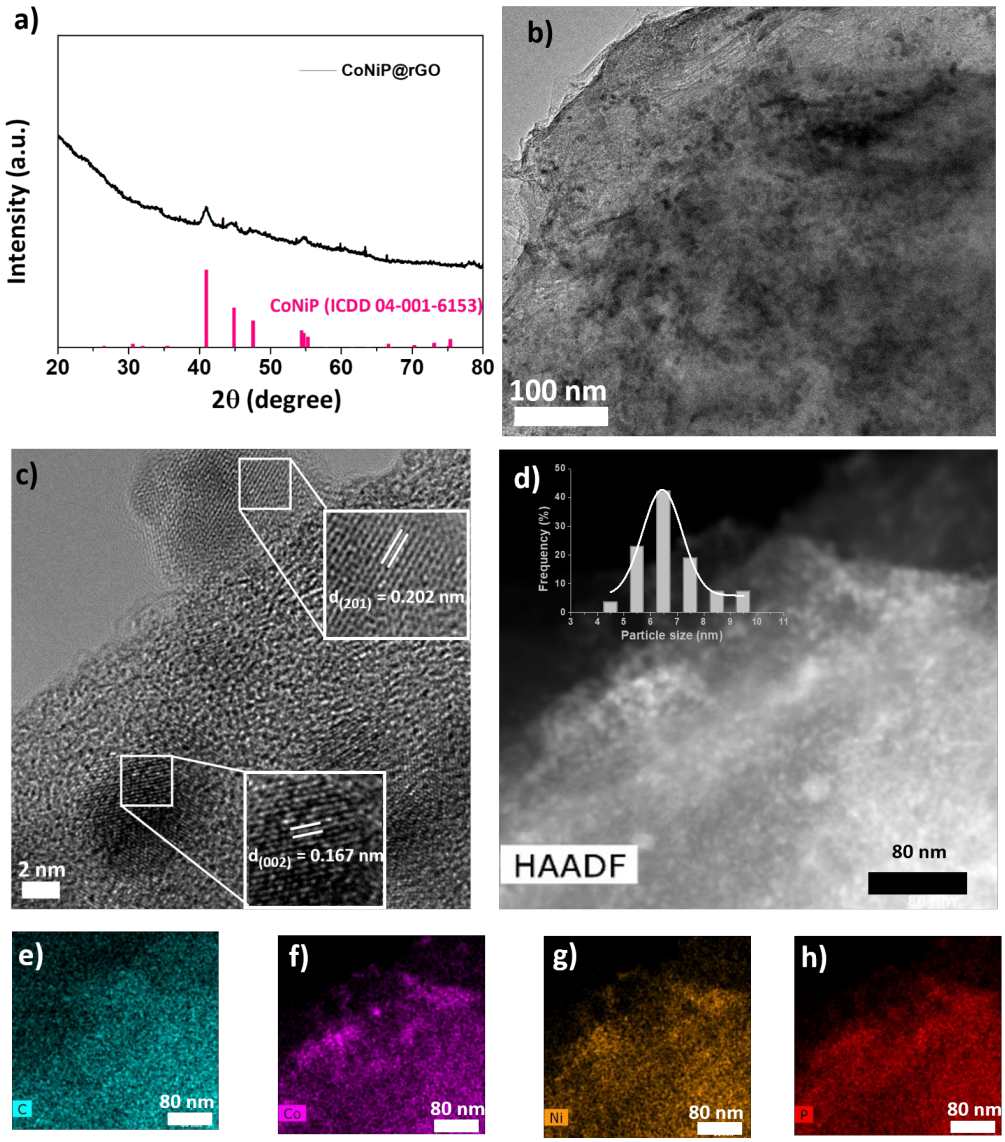

Figure 1. (a) XRD pattern of CoNiP@rGO. The standard powder diffraction pattern of hexagonal CoNiP (ICDD No. 04-001-6153) is given for reference. (b) TEM image, (c) HRTEM image, (d) STEM-HAADF image of CoNiP@rGO. Inset: histogram showing the size distribution of CoNiP NPs. Elemental maps of (e) C, (f) Co, (g) Ni and (h) P.

Fig. 1b shows a representative low-magnification TEM image of CoNiP@rGO, where dense distributions of NPs on rGO are clearly distinguished. In addition, the HRTEM image confirms the crystalline character of the NPs (**Fig. 1c**), where lattice fringes with interplanar distance of 0.202 nm and 0.167 nm can be resolved, corresponding to the (201) and (002) facets

of hexagonal CoNiP (ICDD no. 04-001-6153), respectively. The CoNiP with nanoparticulate feature with an average size of 6.4 nm (**Fig. 1d, inset**) and its high-density distribution on rGO can also be seen clearly in the high-angle annular dark-field scanning transmission electron microscopy (HAADF-STEM) mode (**Fig. 1d**). The elemental mapping (**Fig. 1e-h**) confirms the presence of Co, Ni and P elements and that all elements cover the rGO surface uniformly.

The surface chemical states of CoNi@rGO precursor and CoNiP@rGO were investigated by XPS. The XPS analysis of CoNi@rGO precursor (**Fig. S3**) revealed that this material is mainly in the hydroxide form. The O 1s spectrum can be fitted in four main peaks. The peak at 530.8 and 531.6 eV can be ascribed to the metal-oxygen and metal-hydroxide bond[46, 47], respectively, indicating the presence of cobalt and/or nickel hydroxide. The peak at 532.3 eV is related with carbon–oxygen bonds in rGO [48, 49], while the one at 535.7 eV may be related with adsorbed H_2O[50]. The Co 2p deconvolution spectrum revealed two peaks centered at 781.3 and 785.2 eV which were attributed to Co^{2+} of hydroxide phase and satellite peak, respectively[46]. In the Ni 2p spectrum, two kinds of nickel species containing Ni^{2+} and Ni^{3+} can also be observed at 855.8 and 857.6 eV, respectively, showing the presence of $Ni(OH)_2$ and NiOOH[51, 52].

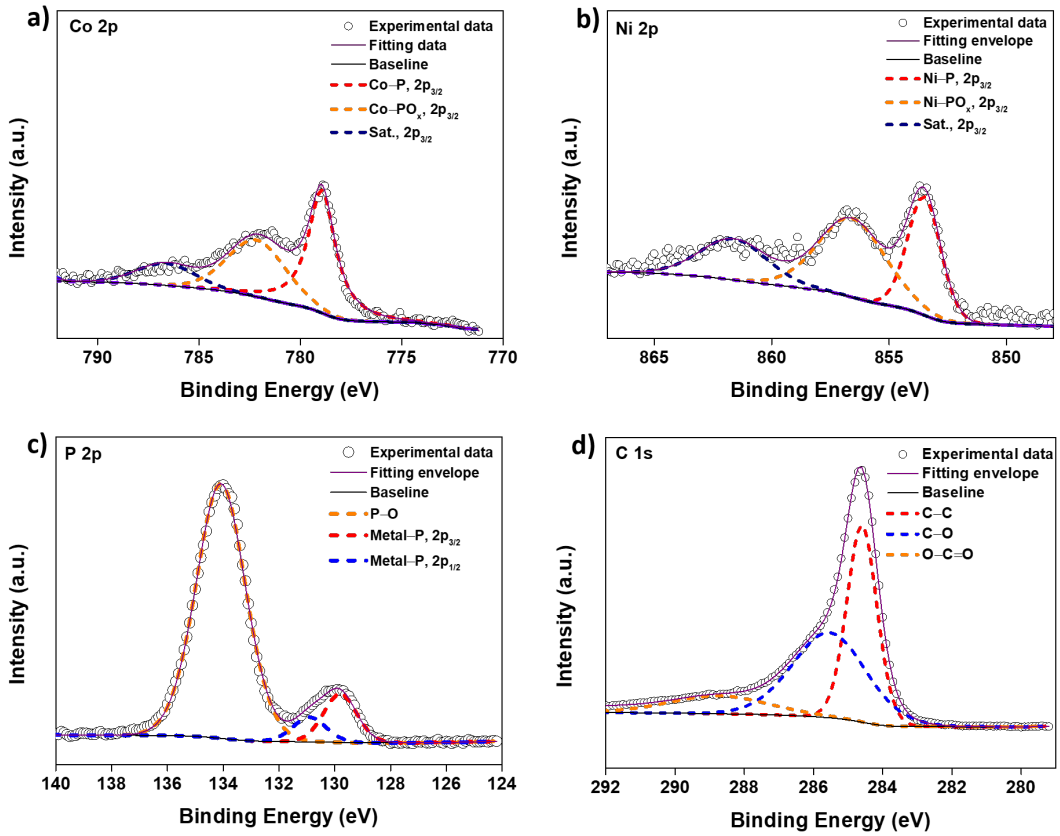

Figure 2. High-resolution XPS spectra of (a) Co 2p, (b) Ni 2p, (c) P 2p and (d) C 1s of CoNiP@rGO.

For CoNiP@rGO, the XPS survey spectra confirm the presence of corresponding elements (**Fig. S4**). The high-resolution Co 2p XPS spectrum (**Fig. 2a**) shows two binding energy (BE) peaks at 778.9 and 782.1 eV as well as a shakeup satellite peak. The characteristic BE peak at 778.9 eV normally relates to the Co 2p component of metal phosphides[53, 54], which is a good indication of Co–P bond formation; whereas the peak at 782.1 eV likely arises from the oxidized Co species, which is related to Co–PO_x[54]. For the Ni 2p spectrum (**Fig. 2b**), the peaks appearing at 853.5 and 856.6 eV can be assigned to the Ni components in phosphides and the oxidized Ni species, respectively [55]. The corresponding satellite peak of Ni $2p_{3/2}$ is centered at 861.6 eV[56]. As far as the P 2p spectrum is concerned (**Fig. 2c**), the two BE peaks appearing at 129.9 and 130.8 eV may be assigned to the P $2p_{3/2}$ and P $2p_{1/2}$ components of metal phosphide, respectively, further confirming the formation of the metal−P bond in the phosphide, while the peak at 134.1 eV is typical of phosphate species[55]. In addition, for the C 1s spectrum of

CoNiP@rGO (**Fig. 2d**) the sp^2-hybridised graphitic carbon (C−C bond) is dominant at 284.6 eV[57]. The other two peaks at 285.5 eV and 288.7 eV can be assigned to C−O and O−C=O, respectively[58]. The weakened intensity of the oxygen-containing bonds in CoNiP@rGO compared to the C 1s spectrum of GO (**Fig. S5**), suggests that GO is reduced to a great extent. Furthermore, the existence of an interaction between the metal phosphide and rGO trough a synergistic effect was confirmed by XPS. As shown in **Fig. S6**, the Co $2p_{3/2}$, Ni $2p_{3/2}$ and P $2p_{3/2}$ binding energies of CoNiP@rGO are positively shifted by 0.4, 0.2 and 0.4 eV, respectively, in comparison to those of unsupported CoNiP, indicating a charge transfer from CoNiP to rGO. This leads to the formation of high-valence-state TMP species with greater oxidizing power.

It is also worth mentioning that after phosphorization treatment at 300 ºC, the intensity of the oxygen-containing bonds of CoNiP@rGO decreased, as shown in the C 1s high-resolution spectrum (**Fig. 2d)**, suggesting a higher degree of reduction of rGO in CoNiP@rGO than that in CoNi@rGO (**Fig. S3d**).

EIS can provide important information about the interfacial behavior of the electrodes, where the semicircle at higher frequencies corresponds to the electron-transfer limited process, and the linear portion at lower frequencies represents the diffusion-limited process [59]. As shown in **Fig. 3a** small semicircle domains were observed on graphene modified electrodes, namely rGO/GCE, CoNi@rGO/GCE and CoNiP@rGO/GCE suggesting their low charge-transfer resistance (R_{ct}) with respect the unsupported materials. After fitting with a Randles equivalent circuit (**Fig. S7**), a R_{ct} value of only 4.2 Ohm was obtained for CoNiP@rGO (**Table 1**), indicating its favorable charge transfer kinetics.

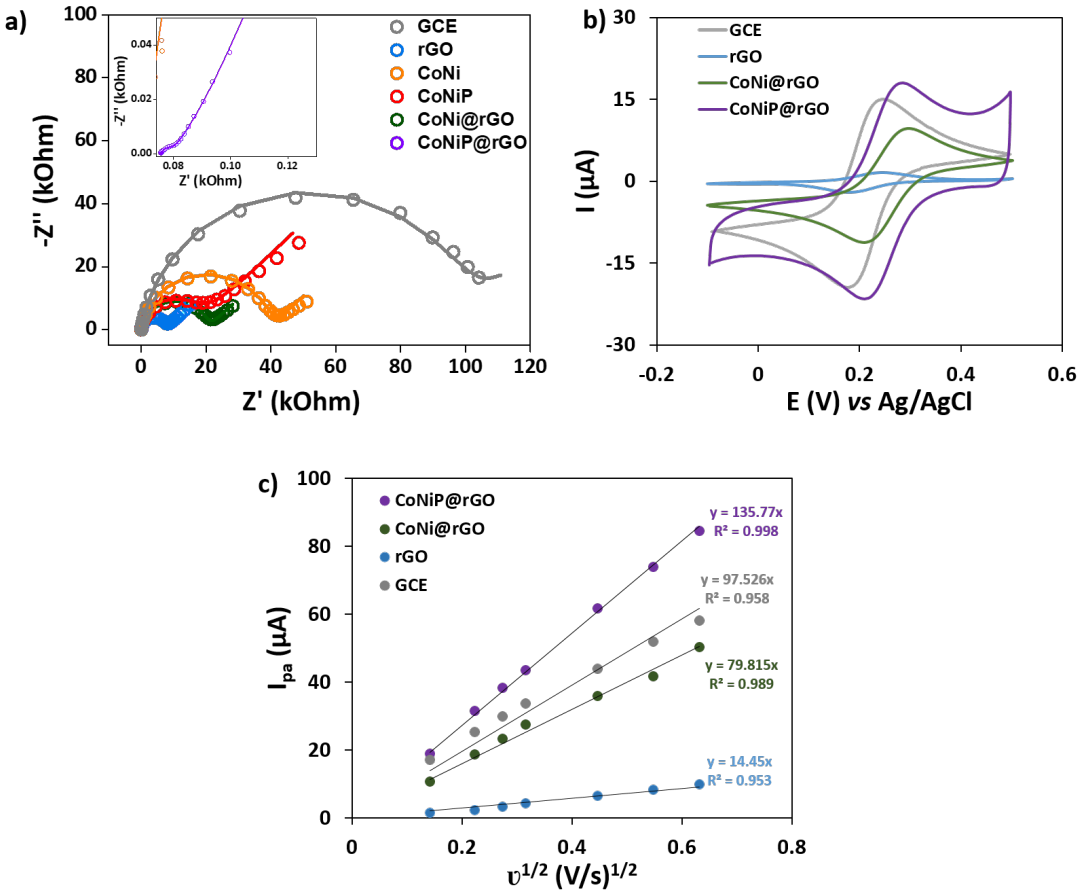

Figure 3. a) Nyquist plots collected in 0.1 M PBS in the presence of 0.5 mM HQ. The inset represents the zoom-in Nyquist plot of CoNiP@rGO/GCE. Scattered dots are experimental data points and solid lines are fitting curves. (b) Cyclic voltammograms of bare GCE, rGO, CoNi@rGO and CoNiP@rGO recorded at a scan rate of 0.02 V s^{-1} in 0.1 M KCl in the presence of 3.0 mM $K_3[Fe(CN)_6]$. (c) I_{pa} vs the square root of υ.

All materials were examined by cyclic voltammetry (CV) using 3.0 mM $K_3[Fe(CN)_6]$ as a redox probe in 0.1 M KCl electrolyte. The ferrocene redox system is often used as a reference probe to study the electrochemical properties of electrocatalysts[60] due to its standard one-electron transfer in the reversible oxidation-reduction process, displaying a high electron transfer rate. As shown in **Fig. 3b**, all materials containing rGO present a well-defined electrochemical response characteristic of a one-electron reversible system: a pair of redox peaks; the peak current ratio of the reverse to the forward scans is equal to unity ($I_{pc}/I_{pa} = 1.0$, where I_{pc} and I_{pa} are the peak current of cathodic and anodic reactions, respectively); the peak-to-peak separation, ΔE_p, is very close to 60 mV. In contrast, the materials synthesized in the

absence of rGO, namely the unsupported CoNi and CoNiP, did not show a reversible redox behavior (data not shown here), since for CoNi the I_{pc}/I_{pa} was lower to unity, while for CoNiP the cathodic peak completely disappeared as shown on **Fig. S8**. Moreover, the results from unsupported CoNiP displayed low reproducibility, which could be due to the dissolution of the material during the consecutive potential cycling. The dissolution may be prevented for the other materials, due to the strong adsorption capacity of GO[61], which functional groups can coordinate with the TM cations, resulting in a desirable binding force to stabilize the as-grown active composite[13, 62]. Moreover, from **Fig. 3b** it is possible to observe that the peak currents obtained for rGO/GCE are lower than that for unmodified GCE. A similar result was previously reported by Pumera and his group[63]. This result may be explained by the fact that in the first step of reduction in the materials synthesis, the GO is only partially reduced by $NaBH_4$, where the sp^2 binding nature of carbon atoms is disrupted by the presence of oxygen-containing groups[63, 64]. Additionally, the electronic/electrostatic repulsion between the negatively charged ferro/ferricyanide probe and the oxygen functionalities can also contribute for the lower current of rGO[63].

The electroactive surface area (ESA) of the graphene modified electrodes was estimated by the I_p according to the Randles-Sevcik equation[38] ($I_p = 2.69\times10^5 \times n^{3/2}AD^{1/2}\,v^{1/2}C$), where n is the number of electrons taking part in the redox reaction (n = 1 for one-electron transfer reaction), A stands for the electroactive surface area (in cm^2), D is the diffusion coefficient ($D = 7.6 \times 10^{-6}$ cm^2 s^{-1} in 0.1 M KCl)[65], C represents the bulk concentration of $K_3[Fe(CN)_6]$ (in mol cm^{-3}), and v is the scan rate (in V s^{-1}). From results shown in **Fig. 3c** the ESA of CoNiP@rGO electrode was calculated to be 6.2 mm^2, which is higher than that of CoNi@rGO (3.6 mm^2), rGO (0.66 mm^2) and bare GCE (4.4 mm^2). The low ESA obtained for rGO and CoNi@rGO is a consequence of the lower peak current obtained for these materials due to the reasons mentioned above.

Electrochemical activity toward HQ

In order to characterize the electrochemical sensing properties towards hydroquinone

detection, cyclic voltammograms were recorded for CoNi/GCE, CoNiP/GCE, CoNi@rGO/GCE, CoNiP@rGO/GCE as well as for rGO/GCE and bare GCE in 0.1 M PBS solution containing 0.5 mM HQ. The background currents of the modified and unmodified GCE are presented in **Fig. S9**, where no visible redox peaks are detected with the exception of rGO that shows a small oxidation peak around +0.7 V.

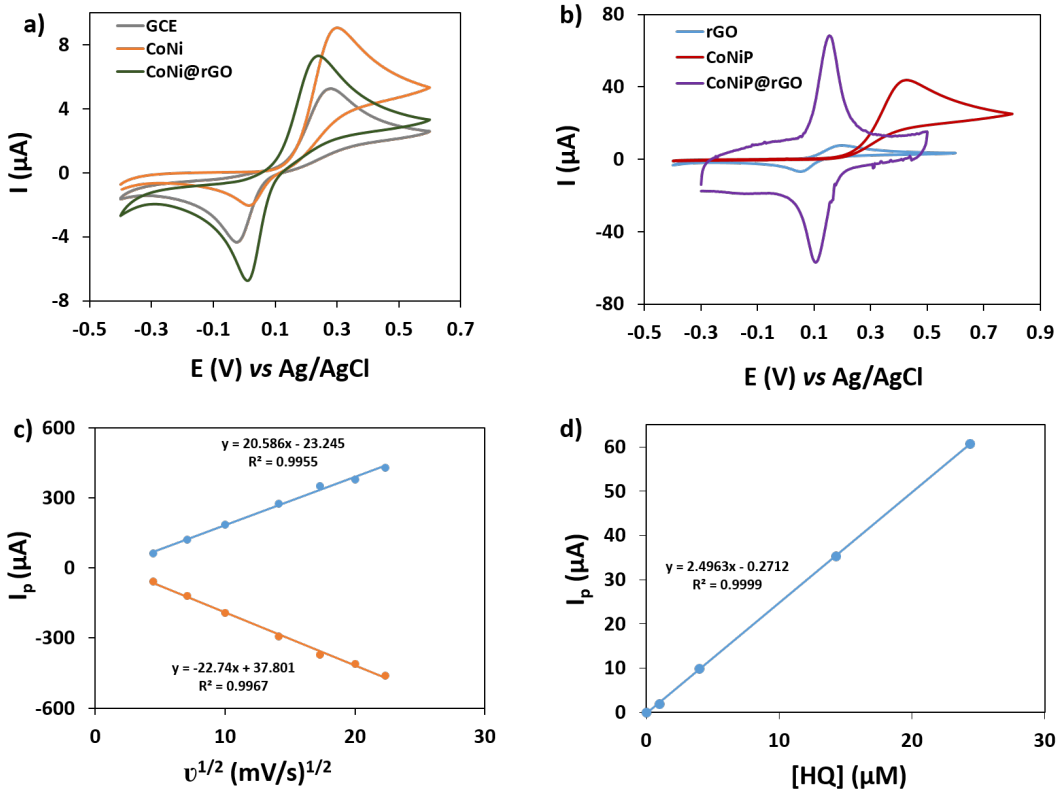

Figure 4. Cyclic voltammograms of (a) bare GCE, CoNi/GCE and CoNi@rGO/GCE, (b) rGO/GCE, CoNiP/GCE and CoNiP@rGO/GCE recorded at a scan rate of 0.02 V s^{-1} in 0.1 M PBS containing 0.5 mM HQ. (c) Plots of peak current intensity vs the square root of υ for CoNiP@rGO/GCE. (d) Peak currents as a function of HQ concentrations, of CoNiP@rGO obtained from DPV.

As shown in **Fig. 4a**, in the presence of HQ a pair of broad redox peaks related with the electrochemical redox reaction of the hydroquinone involving two electrons and two protons (**Scheme 1**) is observed for bare GCE with low peak currents, indicating that GCE is not suitable for highly sensitive sensing of HQ. After modification with CoNi an increment of anodic current occurs, but a decrease in cathodic current can be observed, indicating that the electrochemical reaction taking place on the unsupported CoNi precursor is not reversible.

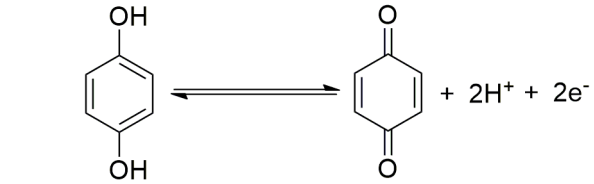

Scheme 1. The electrochemical oxidation of hydroquinone.

After phosphorization treatment of the CoNi precursor to obtain CoNiP, it is possible to observe a sharp increase in the oxidation current (**Fig. 4b**), however, the peak potential is shifted to a higher value and the cathodic peak cannot be detected at all. When Co and Ni were incorporated onto rGO (CoNi@rGO/GCE), in addition to the current increase, a displacement of the peak positions is observed, resulting in a decrease in ΔE_p (**Table 1**) when compared with GCE. The presence of rGO seems to favor the rate of charge transfer as the lower values of ΔE_p were found for all materials containing rGO. On the other hand, a prominent improvement of the electrochemical response was observed for the CoNiP@rGO/GCE electrode, with remarkably higher redox peak currents, which are 10 times higher than that of CoNi@rGO, and a lower anodic peak position (**Fig. 4b**).

The increase of the anodic peak and simultaneous decrease (or absence) of the reduction peak for unsupported CoNi/GCE and CoNiP/GCE may be indicative of a catalytic mechanism[66] that we hypothesize is related to the homogeneous reaction between the benzoquinone (BQ) generated by the HQ (**Eq. (1)**) and the metal components of the electrode material, as represented by **Eq. (2)**, where the decrease of the cathodic (reverse) peak is associated with the consumption of BQ in the chemical reaction with the metal components of CoNi/GCE and CoNiP/GCE, and the increase of the anodic (forward) peak is related to the recovery of HQ by the coupled homogeneous reaction with simultaneous oxidation of the metal centers, represented as $[CoNi(P)]_{ox}$ in **Eq. (2)**.

$$HQ \leftrightarrows BQ + 2H^+ + 2e^- \quad \textbf{(1)}$$

$$2H^+ + BQ + [CoNi(P)] \rightarrow HQ + [CoNi(P)]_{ox} \quad \textbf{(2)}$$

Moreover, by comparison of **Figs. 4a** and **4b** it can be observed that both the decrease of

the cathodic peak and increase of the anodic peak are more prominent for the CoNiP with respect to CoNi, suggesting that the presence of P in the material may increase the rate of the homogeneous reaction. A possible explanation may be related with the fact that in TMPs, the P atom is negatively charged and can act as absorption sites for positively charged H protons, serving as a proton-acceptor center for hydrogen evolution reaction [67]. Therefore, the P atoms can trap the H^+ released during the electrochemical reaction, increasing the protons concentration at the electrode surface, thus improving the kinetics of the chemical reaction, which may explain the pronounced catalytic effect observed for CoNiP modified electrodes.

The behavior of CoNiP in the $Fe^{3+/}Fe^{4+}$ system (**Fig. S8**) is similar to the above described for HQ, where only the oxidation peak is visible with a current intensity that is 2 times higher than that of CoNiP@rGO where the $Fe^{3+/}Fe^{4+}$ system exhibits a reversible response. Therefore, a catalytic mechanism may also justify the voltammetric response of CoNiP in this redox probe.

The incorporation of rGO in both materials, CoNi and CoNiP, has a similar outcome in suppressing the catalytic effect in a large extent, as confirmed by the I_{pc}/I_{pa} ratio (**Table 1**) close to unity for both CoNi@rGO and CoNiP@rGO. The presence of rGO in the catalyst material may stabilize the metal centers by synergistic effect between the TM(P) and rGO[14, 68]. As mentioned above, the modulation of the electronic structure of TMP can be observed by the BE blue shift of the metal components in CoNiP@rGO compared with CoNiP (**Fig. S6**). As the electron density of metal centers in CoNiP@rGO decreases it already shows higher-valence-states ($[CoNiP]_{ox}$@rGO) with respect to that of CoNiP, inhibiting the charge transference between CoNiP and BQ in **Eq. (2)**.

For the materials where the catalytic effect did not occur, namely rGO/GCE and CoNi@rGO/GCE, the observed current increase compared to that of GCE cannot be simply explained by the variation of the electroactive surface area of the catalyst since the ESA decreases (estimated by the Randles-Sevcik equation) by 84% and 18%, respectively. Instead, the I_p increase may be related to the increase in the rate of electron transfer to the HQ, which can be positively affected by the formation of hydrogen bonds between the rGO functional groups (C=O and C−OH) and HQ/BQ redox system, as reported before by Gusmão *et al*. [69, 70]. With respect to CoNiP@rGO/GCE, the ESA can only partially explain the current increase

since the increase of the ESA is only about 39% from bare GCE to CoNiP@rGO/GCE, while the increase of I_p is around 1255%. The characteristics of the voltammogram of CoNiP@rGO/GCE (lower values of peak potentials, ΔE_p and $E_{pa} - E_{pa/2}$, where $E_{pa/2}$, stands for half-wave potential peak) suggest that this effect is mainly due to an effective increase in the rate of electron transfer, which was also confirmed by EIS results (**Fig. 3a**) where the low R_{ct} value of CoNiP@rGO/GCE justifies the faster kinetics of the electrochemical reaction of HQ facilitated by the rapid electron transport at the electrode/electrolyte interface. Moreover, the effect of scan rate on the HQ redox peak current was studied for CoNiP@rGO/GCE (**Fig. 4c**), showing that the peak current increases steadily with the scan rate from 20 to 400 mV s^{-1}. The linear relationship between peak current intensity (I_p) and the square root of scan rate ($v^{1/2}$) implies that the HQ oxidation at CoNiP@rGO is a diffusion-controlled process. This result points out that the good performance of CoNiP@rGO does not originate from the adsorption of HQ.

Further, DPV was employed to detect different standard concentrations of HQ using CoNiP@rGO/GCE sensor. The results showed that the anodic peak current was linear to the concentration of HQ, exhibiting a high linear correlation coefficient (**Fig. 4d**). The high slope of the trendline suggests a large sensitivity (around 35.7 A^{-1} M^{-1} cm^{-2}), suggesting that CoNiP@rGO could be a promising candidate for the determination of HQ. The catalytic activity of CoNiP@rGO/GCE promoted by the rGO support may be explained considering the higher surface area of rGO that enables the metal nanoparticles to nucleate avoiding their agglomeration during the post-treatment, offering a more homogeneous surface with active sites for the HQ oxidation. Furthermore, the synergistic effect between the electrocatalytic activity of CoNiP and the highly conductive rGO, as confirmed by XPS results (**Fig. S6**) may have contributed to the catalytic performance. Moreover, both the larger electroactive surface area and the lower electron-transfer resistance, as well as the proton-acceptor character of P atoms in CoNiP@rGO, boost the high sensitivity for HQ detection.

Table 1. Comparison between I_{pc}/I_{pa}, ΔE_p and $E_{pa} - E_{pa/2}$ for all the electrodes and the corresponding electrode's R_{ct} and ESA values

	I_{pa} (µA)	I_{pc} (µA)	I_{pc}/I_{pa}	E_{pa} (mV)	E_{pc} (mV)	ΔE_p	E_{pa}-$E_{pa/2}$ (V)	R_{ct} (kOhm)	ESA (mm^2)
GCE	4.67	-4.44	0.95	278	-24	302	77.7	96.6	4.4
CoNi/GCE	6.80	-1.71	0.25	290	20.4	269.6	79.6	39.6	n.d
CoNiP/GCE	41.3	0	0	424	-	-	98.5	17.3	n.d
rGO/GCE	7.26	-7.11	0.98	194	54	140	70.0	7.33	0.66
CoNi@rGO/GCE	6.32	-6.18	0.98	236	12	224	73.0	20.0	3.6
CoNiP@rGO/GCE	63.3	-58.8	0.93	142	94	48	37.9	0.0042	6.2

Conclusions

Different materials were prepared based on bimetallic transition metals and the effect of the different material components, namely the presence of phosphorus and rGO, on the electrochemical response towards HQ detection, was studied. The experimental results show that CoNiP@rGO exhibit markedly improved electrochemical response in terms of peak current and peak position, when compared to the samples in the absence of P and/or rGO. Moreover, the presence of rGO provides an optimized structural architecture since it can help to avoid the agglomeration and dissolution of CoNiP, offering larger surface areas and more active sites. Furthermore, the synergetic interaction between CoNiP and rGO helps to modulate the electronic structure and contributes to the enhanced catalytic performance of CoNiP@rGO. In addition, the proton-acceptor behavior of P atoms and the ability of rGO to form hydrogen bonds with HQ/BQ system also result in the enhanced electrocatalytic ability of HQ sensing. Our work provides a guidance in the design of a multicomponent electrocatalyst with potential

applications in electrochemical sensing of phenolic compounds, and our CoNiP@rGO can serve as a promising platform for electrochemical sensors construction.

Acknowledgments

Thanks are due to Fundação para a Ciência e Tecnologia (FCT) and FEDER (European Fund for Regional Development)-COMPETE-QRENEU for financial support through the research units Chemistry Research Centre of (UID/QUI/00686/2020). This work was carried out in part using the Advanced Electron Microscopy, Imaging and Spectroscopy (AEMIS) Facilities available at INL. I. Amorim is thankful to Fundação para a Ciência e Tecnologia (FCT) for the support of PhD grant No. SFRH/BD/137546/2018, co-financed by the Fundo Social Europeu (FSE) through the Programa Operacional Regional Norte (Norte 2020) under Portugal 2020.

References

1. F. Pino, C. C. Mayorga-Martinez, and A. Merkoci, *Electrochem Commun,* **71** 33-37 (2016).
2. G. H. Zheng, Y. Y. Zhang, T. M. Nie, X. M. Jiang, Q. J. Wan, Y. W. Li, and N. J. Yang, *Sensor Actuat B-Chem,* **291** 362-368 (2019).
3. M. Sakthivel, S. Ramaraj, S. M. Chen, B. Dinesh, H. V. Ramasamy, and Y. S. Lee, *Anal Chim Acta,* **1006** 22-32 (2018).
4. Y. H. Duan, S. Li, S. Lei, J. T. Qiao, L. N. Zou, and B. X. Ye, *J Electroanal Chem,* **827** 137-144 (2018).
5. S. P. Wang, Z. Han, Y. F. Li, R. F. Peng, and B. Feng, *Rsc Adv,* **5** (130), 107318-107325 (2015).
6. A. Agarwal and B. R. Sankapal, *J Mater Chem A,* **9** (36), 20241-20276 (2021).
7. Y. B. Lian, H. Sun, X. B. Wang, P. W. Qi, Q. Q. Mu, Y. J. Chen, J. Ye, X. H. Zhao, Z. Deng, and Y. Peng, *Chem Sci,* **10** (2), 464-474 (2019).
8. X. X. Ma, Y. Q. Chang, Z. Zhang, and J. L. Tang, *J Mater Chem A,* **6** (5), 2100-2106 (2018).
9. A. Han, H. Y. Zhang, R. H. Yuan, H. X. Ji, and P. W. Du, *Acs Appl Mater Inter,* **9** (3), 2240-2248 (2017).
10. N. Zhang, J. Y. Xu, B. Wei, J. J. Li, I. Amorim, R. Thomas, S. M. Thalluri, Z. C. Wang, W. Y. Zhou, S. S. Xie, and L. F. Liu, *ACS Appl Energ Mater,* **3** (5), 4580-4588 (2020).
11. X. J. Chen, M. Cheng, D. Chen, and R. M. Wang, *Acs Appl Mater Inter,* **8** (6), 3892-3900 (2016).
12. N. Zhang, Y. F. Li, J. Y. Xu, J. J. Li, B. Wei, Y. Ding, I. Amorim, R. Thomas, S. M. Thalluri, Y. Y. Liu, G. H. Yu, and L. F. Liu, *Acs Nano,* **13** (9), 10612-10621 (2019).
13. C. Jing, X. Y. Song, K. L. Li, Y. M. Zhang, X. Y. Liu, B. Q. Dong, F. Dong, S. L. Zhao, H. C. Yao, and Y. X. Zhang, *J Mater Chem A,* **8** (4), 1697-1708 (2020).
14. X. X. Zhao, Y. P. Fan, H. Y. Wang, C. Y. Gao, Z. Y. Liu, B. J. Li, Z. K. Peng, J. H. Yang, and

B. Z. Liu, *Acs Omega,* **5** (12), 6516-6522 (2020).
15. B. Koo, S. Byun, S. W. Nam, S. Y. Moon, S. Kim, J. Y. Park, B. T. Ahn, and B. Shin, *Adv Funct Mater,* **28** (16), (2018).
16. P. Murugan, R. D. Nagarajan, A. K. Sundramoorthy, D. Ganapathy, R. Atchudan, D. Nallaswamy, and A. Khosla, *ECS Sensors Plus,* **1** (3), 034401 (2022).
17. S. Singh, J. Wang, and S. Cinti, *ECS Sensors Plus,* **1** (2), 023401 (2022).
18. T. T. T. Toan and D. M. Nguyen, *ECS Sensors Plus,* **1** (2), 021604 (2022).
19. V. Chabot, D. Higgins, A. P. Yu, X. C. Xiao, Z. W. Chen, and J. J. Zhang, *Energ Environ Sci,* **7** (5), 1564-1596 (2014).
20. D. M. Nguyen and T. T. T. Toan, *ECS Sensors Plus,* **1** (3), 031603 (2022).
21. V. Agarwal and P. B. Zetterlund, *Chem Eng J,* **405** 127018 (2021).
22. L. J. Liu, R. F. Chen, W. K. Liu, J. M. Wu, and D. Gao, *J Hazard Mater,* **320** 96-104 (2016).
23. Q. Q. Sun, M. Wang, S. J. Bao, Y. C. Wang, and S. Gu, *Analyst,* **141** (1), 256-260 (2016).
24. T. Chen, D. Liu, W. B. Lu, K. Y. Wang, G. Du, A. M. Asiri, and X. P. Sun, *Analytical Chemistry,* **88** (16), 7885-7889 (2016).
25. L. S. Xie, A. M. Asiri, and X. P. Sun, *Sensor Actuat B-Chem,* **244** 11-16 (2017).
26. Y. Y. Zhu, Y. L. Wang, K. Kang, Y. L. Lin, W. Guo, and J. Wang, *Microchim Acta,* **187** (2), 100 (2020).
27. Z. Li, Y. Xin, W. Wu, B. Fu, and Z. Zhang, *Anal Chem,* **88** (15), 7724-7729 (2016).
28. X. L. Xiong, C. You, X. Q. Cao, L. F. Pang, R. M. Kong, and X. P. Sun, *Electrochim Acta,* **253** 517-521 (2017).
29. D. H. Yin, J. Y. Tang, R. B. Bai, S. Y. Yin, M. N. Jiang, Z. G. Kan, H. M. Li, F. Wang, and C. L. Li, *Nanoscale Res Lett,* **16** (1), 11 (2021).
30. S. J. Tong, Z. Z. Li, B. L. Qiu, Y. N. Zhao, and Z. H. Zhang, *Sensor Actuat B-Chem,* **258** 789-795 (2018).
31. M. Wei, W. B. Lu, M. Zhu, R. Zhang, W. L. Hu, X. W. Cao, J. F. Jia, and H. S. Wu, *J Mater Sci,* **56** (10), 6401-6410 (2021).
32. X. Zhang, Y. C. Zhang, and J. W. Zhang, *Talanta,* **161** 567-573 (2016).
33. H. Wang, Y. D. Chi, X. H. Gao, S. Lv, X. F. Chu, C. Wang, L. Zhou, and X. T. Yang, *J Chem-Ny,* 2346895 (2017).
34. H. F. Zhou, M. L. Cui, Y. Zhao, C. Wang, and Q. J. Song, *Electrochim Acta,* **242** 107-116 (2017).
35. L. L. Xiao, R. Y. Xu, and F. Wang, *Talanta,* **179** 448-455 (2018).
36. K. D. Wang, C. Wu, F. Wang, and G. Q. Jiang, *Acs Applied Nano Materials,* **1** (10), 5843-5853 (2018).
37. X. B. Liu, F. Y. He, L. W. Bai, X. W. Cao, C. Liu, and W. B. Lu, *Anal Chim Acta,* **1210** 339871 (2022).
38. H. Guo, Y. L. Shen, H. Y. Ouyang, Y. M. Long, and W. F. Li, *Microchim Acta,* **186** (12), 819 (2019).
39. D. D. Yin, J. Liu, X. J. Bo, and L. P. Guo, *Anal Chim Acta,* **1093** 35-42 (2020).
40. W. W. Anku, M. A. Mamo, and P. P. Govender, in *Phenolic Compounds - Natural Sources, Importance and Applications*, M. Soto-Hernandez, M. Palma-Tenango and M. d. R. Garcia-Mateos, eds., p. 17, InTech, Rijeka, (2017).
41. R. Umapathi, S. M. Ghoreishian, G. M. Rani, Y. Cho, and Y. S. Huh, *ECS Sensors Plus,* **1** (4), 044601

(2022).
42. A. Meng, H. Q. Zhang, B. H. Huangfu, W. L. Tian, L. Y. Sheng, Z. J. Li, S. Q. Tan, and Q. D. Li, *Prog Nat Sci-Mater,* **30** (4), 461-468 (2020).
43. H. F. Liang, A. N. Gandi, D. H. Anjum, X. B. Wang, U. Schwingenschlogl, and H. N. Alshareef, *Nano Lett,* **16** (12), 7718-7725 (2016).
44. N. Zhang, Y. F. Li, J. Y. Xu, J. J. Li, B. Wei, Y. Ding, I. Arnorim, R. Thomas, S. M. Thalluri, Y. Y. Liu, G. H. Yu, and L. F. Liu, *Acs Nano,* **13** (9), 10612-10621 (2019).
45. J. Y. Xu, J. J. Li, D. H. Xiong, B. S. Zhang, Y. F. Liu, K. H. Wu, I. Amorim, W. Li, and L. F. Liu, *Chem Sci,* **9** (14), 3470-3476 (2018).
46. N. Naseri, A. Esfandiar, M. Qorbani, and A. Z. Moshfegh, *Acs Sustain Chem Eng,* **4** (6), 3151-3159 (2016).
47. X. J. Li, Y. C. Tang, J. X. Zhu, H. M. Lv, L. M. Zhao, W. L. Wang, C. Y. Zhi, and H. F. Li, *Small,* **16** (31), 2001935 (2020).
48. S. L. Luo, L. Qian, M. L. Liao, X. R. Hu, and D. Xiao, *Rsc Adv,* **7** (72), 45294-45303 (2017).
49. J. V. Rojas, M. Toro-Gonzalez, M. C. Molina-Higgins, and C. E. Castano, *Mater Sci Eng B-Adv,* **205** 28-35 (2016).
50. H. J. L. Clabel, V. A. G. Rivera, M. S. Li, L. A. O. Nunes, E. R. Leite, W. H. Schreiner, and E. Marega, *J Alloy Compd,* **619** 800-806 (2015).
51. S. F. Zhang, A. Pei, G. Li, L. H. Zhu, G. D. Li, F. S. Wu, S. T. Lin, W. Q. Chen, B. H. Chen, and R. Luque, *Green Chem,* **24** (6), 2438-2450 (2022).
52. B. Li, K. F. Wang, J. X. Ren, and P. Qu, *New J Chem,* **46** (16), 7615-7625 (2022).
53. Y. Li, B. Wei, Z. P. Yu, O. Bondarchuk, A. Araujo, I. Amorim, N. Zhang, J. Y. Xu, I. C. Neves, and L. F. Liu, *Acs Sustain Chem Eng,* **8** (27), 10193-10200 (2020).
54. L. Han, T. W. Yu, W. Lei, W. W. Liu, K. Feng, Y. L. Ding, G. P. Jiang, P. Xu, and Z. W. Chen, *J Mater Chem A,* **5** (32), 16568-16572 (2017).
55. Y. P. Li, J. D. Liu, C. Chen, X. H. Zhang, and J. H. Chen, *Acs Appl Mater Inter,* **9** (7), 5982-5991 (2017).
56. X. Zhang, J. W. Li, Y. F. Sun, Z. J. Li, P. Liu, Q. Y. Liu, L. Tang, and J. X. Guo, *Electrochim Acta,* **282** 626-633 (2018).
57. M. Huang, K. Ge, G. D. Dong, Z. H. Zhou, and Y. W. Zeng, *Int J Hydrogen Energ,* **44** (26), 13195-13204 (2019).
58. H. Y. Zheng, X. B. Huang, H. Y. Gao, W. J. Dong, G. L. Lu, X. Chen, and G. Wang, *J Energy Chem,* **34** 72-79 (2019).
59. S. M. Babulal, S. M. Chen, R. Palani, K. Venkatesh, A. S. Haidyrah, S. K. Ramaraj, C. C. Yang, and C. Karuppiah, *Colloid Surface A,* **621** 126600 (2021).
60. N. G. Tsierkezos, *J Solution Chem,* **36** (3), 289-302 (2007).
61. R. R. Amirov, J. Shayimova, Z. Nasirova, A. Solodov, and A. M. Dimiev, *Phys Chem Chem Phys,* **20** (4), 2320-2329 (2018).
62. R. R. Amirov, J. Shayimova, Z. Nasirova, and A. M. Dimiev, *Carbon,* **116** 356-365 (2017).
63. J. G. S. Moo, A. Ambrosi, A. Bonanni, and M. Pumera, *Chem-Asian J,* **7** (4), 759-770 (2012).
64. J. P. Zhao, S. F. Pei, W. C. Ren, L. B. Gao, and H. M. Cheng, *Acs Nano,* **4** (9), 5245-5252 (2010).
65. D. Zhu, Q. F. Zhen, J. J. Xin, H. Y. Ma, L. C. Tan, H. J. Pang, and X. M. Wang, *Sensor Actuat B-Chem,* **321** 128541 (2020).

66. A. J. Bard and L. R. Faulkner, *Electrochemical Methods: Fundamentals and Applications*, Wiley (2000).
67. J. Z. Su, J. L. Zhou, L. Wang, C. Liu, and Y. B. Chen, *Sci Bull,* **62** (9), 633-644 (2017).
68. Z. H. Zhang, C. B. Li, H. R. Huang, J. F. Li, X. Q. Zhang, Z. Y. Li, H. Wei, and H. B. Chu, *Electrochim Acta,* **362** 137172 (2020).
69. R. Gusmao, M. Melle-Franco, D. Geraldo, F. Bento, M. C. Paiva, and F. Proenca, *Electrochem Commun,* **57** 22-26 (2015).
70. R. Gusmao, E. Cunha, C. Paiva, D. Geraldo, F. Proenca, and F. Bento, *Chemelectrochem,* **3** (12), 2138-2145 (2016).